



Identification of Phase Control of Carbon-Confined Nb₂O₅ Nanoparticles toward High-Performance Lithium Storage

Jiashen Meng, Qiu He, Linhan Xu, Xingcai Zhang, Fang Liu, Xuanpeng Wang, Qi Li, Xiaoming Xu, Guobin Zhang, Chaojiang Niu, Zhitong Xiao, Ziang Liu, Zizhong Zhu, Yan Zhao,* and Liqiang Mai*

Niobium pentoxides (Nb₂O₅) have attracted extensive interest for ultrafast lithium-ion batteries due to their impressive rate/capacity performance and high safety as intercalation anodes. However, the intrinsic insulating properties and unrevealed mechanisms of complex phases limit their further applications. Here, a facile and efficient method is developed to construct three typical carbon-confined Nb₂O₅ (TT-Nb₂O₅@C, T-Nb₂O₅@C, and H-Nb₂O₅@C) nanoparticles via a mismatched coordination reaction during the solvothermal process and subsequent controlled heat treatment, and different phase effects are investigated on their lithium storage properties on the basis of both experimental and computational approaches. The thin carbon coating and nanoscale size can endow Nb₂O₅ with a high surface area, high conductivity, and short diffusion length. As a proof-of-concept application, when employed as LIB anode materials, the resulting T-Nb₂O₅@C nanoparticles display higher rate capability and better cycling stability as compared with TT-Nb₂O₅@C and H-Nb₂O₅@C nanoparticles. Furthermore, a synergistic effect is investigated and demonstrated between fast diffusion pathways and stable hosts in T-Nb₂O₅ for ultrafast and stable lithium storage, based on crystal structure analysis, in situ X-ray diffraction analysis, and density functional theoretical calculations. Therefore, the proposed synthetic strategy and obtained deep insights will stimulate the development of Nb₂O₅ for ultrafast and long-life LIBs.

developing advanced electrochemical energy storage devices with high energy/power density and long lifespan.^[1] Among them, lithium-ion batteries (LIBs) and supercapacitors (SCs) are two most promising devices for chemical energy storage.^[2] However, there has been an obvious research boundary between them owing to their different charge-storage mechanisms. Generally, LIBs provide high energy density but relatively low power density on basis of insertion-, conversion-, and alloying-type mechanisms, while SCs exhibit high power density and relatively good cycling stability but low energy density via a fast physisorption and/or shallow redox reaction on the electrode/electrolyte interface.^[3] Therefore, to meet the market need and conquer the energy storage barrier, developing advanced LIBs with supercapacitor-like rate performance that combines both merits is a very challenging research direction with vital importance in the near future.^[4]

There is no doubt that the intrinsic phase structures of electrode materials play a crucial role in improving battery performance.^[5] Compared with conversion-/

alloying-type materials, most insertion-type materials have robust crystalline skeletons and relatively high diffusion efficiency during charging and discharging, which can endow LIBs with long-term cycling stability and high rate capability.^[6]

1. Introduction

To meet the growing market requirements for portable electronics and electric vehicles, researchers have focused on

J. S. Meng, F. Liu, Dr. X. P. Wang, Prof. Q. Li, X. M. Xu, G. B. Zhang, Dr. C. J. Niu, Z. T. Xiao, Z. A. Liu, Prof. L. Q. Mai
State Key Laboratory of Advanced Technology for Materials Synthesis and Processing
Wuhan University of Technology
Wuhan 430070, China
E-mail: mlq518@whut.edu.cn

Q. He, Prof. Y. Zhao
State Key Laboratory of Silicate Materials for Architectures
Wuhan University of Technology
Wuhan 430070, China
E-mail: yan2000@whut.edu.cn

L. H. Xu, Prof. Z. Z. Zhu
Department of Physics and Collaborative Innovation Center for Optoelectronic Semiconductors and Efficient Devices
Xiamen University
Xiamen 361005, China
Dr. X. C. Zhang
John A. Paulson School of Engineering and Applied Sciences
Harvard University
Cambridge, MA 02138, USA

The ORCID identification number(s) for the author(s) of this article can be found under <https://doi.org/10.1002/aenm.201802695>.

DOI: 10.1002/aenm.201802695

Recently, niobium pentoxide (Nb_2O_5) has been considered as a promising anode material for LIBs because of its considerable theoretical capacity ($\approx 200 \text{ mAh g}^{-1}$) and excellent rate capability in the potential range from 1.0 and 2.0 V versus Li^+/Li .^[7] In addition, issues about electrolyte instability and lithium dendrite formation below 1.0 V versus Li^+/Li in anode materials can be efficiently avoided, making batteries much safer. However, the Nb_2O_5 exists in many polymorphic forms, such as TT-, T-, B-, N-, P-, M-, and H- Nb_2O_5 , which have different effects on their lithium storage performance.^[8] For example, Dunn and co-workers demonstrated a pseudocapacitive mechanism in orthorhombic Nb_2O_5 (denoted as T- Nb_2O_5), and revealed that the high rate capability of T- Nb_2O_5 was attributed to the mostly empty octahedral sites between its (001) planes.^[9] Grey and co-workers compared the crystal structures and lithium storage performances of different Nb_2O_5 polymorphs, and found that the monoclinic Nb_2O_5 (denoted as H- Nb_2O_5) displayed higher initial capacity, lower capacity retention, and poorer rate performance than T- Nb_2O_5 , TT- Nb_2O_5 , and B- Nb_2O_5 phases.^[10] Recently, Liu and co-workers revealed the nature of fast Li-ion storage in T- Nb_2O_5 using both in operando Raman spectroscopy and theoretical calculations.^[7b] However, because of their complex structures, it is a great challenge to investigate the origin of the lithium storage properties of different Nb_2O_5 polymorphs so far.

Nb_2O_5 is an electronic insulator with poor electric conductivity ($\approx 3.4 \times 10^{-6} \text{ S cm}^{-1}$ at 300 K), which greatly limits its high-rate capability for LIBs, especially in thick electrodes with high mass loading.^[11] Recently, intensive efforts have been dedicated to developing various strategies to improve the electrochemical performance of Nb_2O_5 . One typical method is to design various Nb_2O_5 nanostructures, such as mesoporous nanobelts, nanosheets, nanoparticles, nanorods, and so on, which can greatly shorten the diffusion distances of both ions and electrons during the cycling performance.^[12] In addition, integrating various carbon materials with Nb_2O_5 nanostructures to form delicate composites is an efficient approach to enhance the electronic conductivity.^[13] For example, Lee and co-workers synthesized carbon-confined TT- and T- Nb_2O_5 core-shell nanocrystals by a facile water-in-oil microemulsion method, which displayed high reversible capacity and rapid rate capability in LIBs.^[14] Duan and co-workers developed a two-step method to design and construct a 3D holey-graphene/ Nb_2O_5 composite for ultrafast lithium storage at high mass loading.^[15] The highly interconnected holey-graphene scaffold endowed the whole electrode with excellent electron/ion transport properties. Therefore, developing unique carbon-based Nb_2O_5 composites via a facile method is highly desired toward high-performance LIBs.

In this paper, we designed and constructed three kinds of carbon-confined Nb_2O_5 nanoparticles (TT- $\text{Nb}_2\text{O}_5@C$, T- $\text{Nb}_2\text{O}_5@C$, and H- $\text{Nb}_2\text{O}_5@C$) by a two-step process, including a mismatched coordination reaction and subsequent in situ carbonization, and systematically investigated the effects of different phases on their lithium storage performances based on both experimental analysis and theoretical calculations. Our design is based on the fact that most polymorphs of Nb_2O_5 are metastable and similar, and TT- Nb_2O_5 , T- Nb_2O_5 , and H- Nb_2O_5 are three most typical and widely studied forms. We have clearly shown that the mismatched coordination reaction results in the formation of amorphous metal–ligand complex precursor nanoparticles. The confined carbon shell provides excellent electron transport property (Figure S1, Supporting Information). When employed in LIB anode materials, the as-prepared T- $\text{Nb}_2\text{O}_5@C$ exhibited higher rate capability and better cycling stability than TT- $\text{Nb}_2\text{O}_5@C$ and H- $\text{Nb}_2\text{O}_5@C$. Furthermore, we carried out crystal structure analysis, in situ X-ray diffraction (XRD) testing and density functional theory calculations to reveal their lithium storage mechanisms.

2. Results and Discussion

As shown in **Figure 1**, the crystal structures of TT- Nb_2O_5 , T- Nb_2O_5 , and H- Nb_2O_5 are first illustrated. In previous reports, both TT- Nb_2O_5 and T- Nb_2O_5 are two low-temperature forms with similar structures.^[10,16] Among them, T- Nb_2O_5 is the most studied one, of which crystal structures have been clearly shown. T- Nb_2O_5 is orthorhombic with a space group of Pbam, and cell parameters of $a = 6.175$, $b = 29.175$, $c = 3.93 \text{ \AA}$. The cell formula of T- Nb_2O_5 is $\text{Nb}_{16.8}\text{O}_{42}$. The detailed crystal structure of T- Nb_2O_5 is composed of mainly highly distorted octahedral (NbO_6) and pentagonal bipyramidal (NbO_7) (16 Nb atoms occupation) framework. The remaining 0.8 Nb atoms are widely distributed into the as-formed crystal framework by high coordination and long Nb–O interatomic distances. Their unique $\text{NbO}_6/\text{NbO}_7$ framework structures like “room-and-pillar” can provide a stable host and easy diffusion channels for lithium intercalation.^[7b] The TT- Nb_2O_5 has a pseudo-hexagonal unit cell with $a = 7.23$, $b = 15.7$, $c = 7.18 \text{ \AA}$, $\beta = 119.5^\circ$. TT- Nb_2O_5 can be considered as a disordering modification of the T- Nb_2O_5 .^[16,17] The cell unit of TT- Nb_2O_5 contains nonstoichiometric $\text{Nb}_{16}\text{O}_{42}$. After removal of the 0.8 Nb positions in T- Nb_2O_5 , the remained Nb atoms become more symmetric, resulting in the formation of Nb positions of TT- Nb_2O_5 at $(x, y, 0.5)$ plane in T- Nb_2O_5 . Thermodynamically, H- Nb_2O_5 is a most stable high-temperature phase. H- Nb_2O_5 is monoclinic with a space group of P2, and

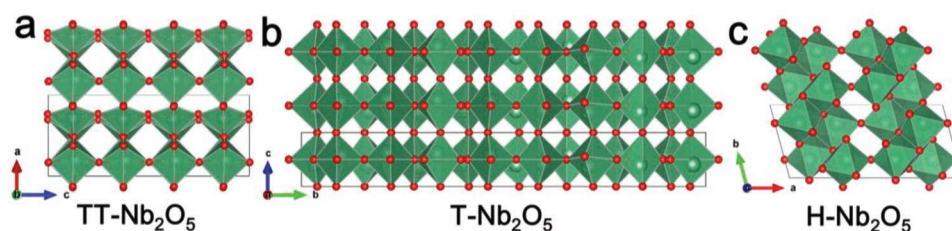


Figure 1. Schematic illustrations of the crystal structures of a) TT- Nb_2O_5 , b) T- Nb_2O_5 , and c) H- Nb_2O_5 , respectively. The red balls represent O atoms; dark cyan balls represent Nb atoms.

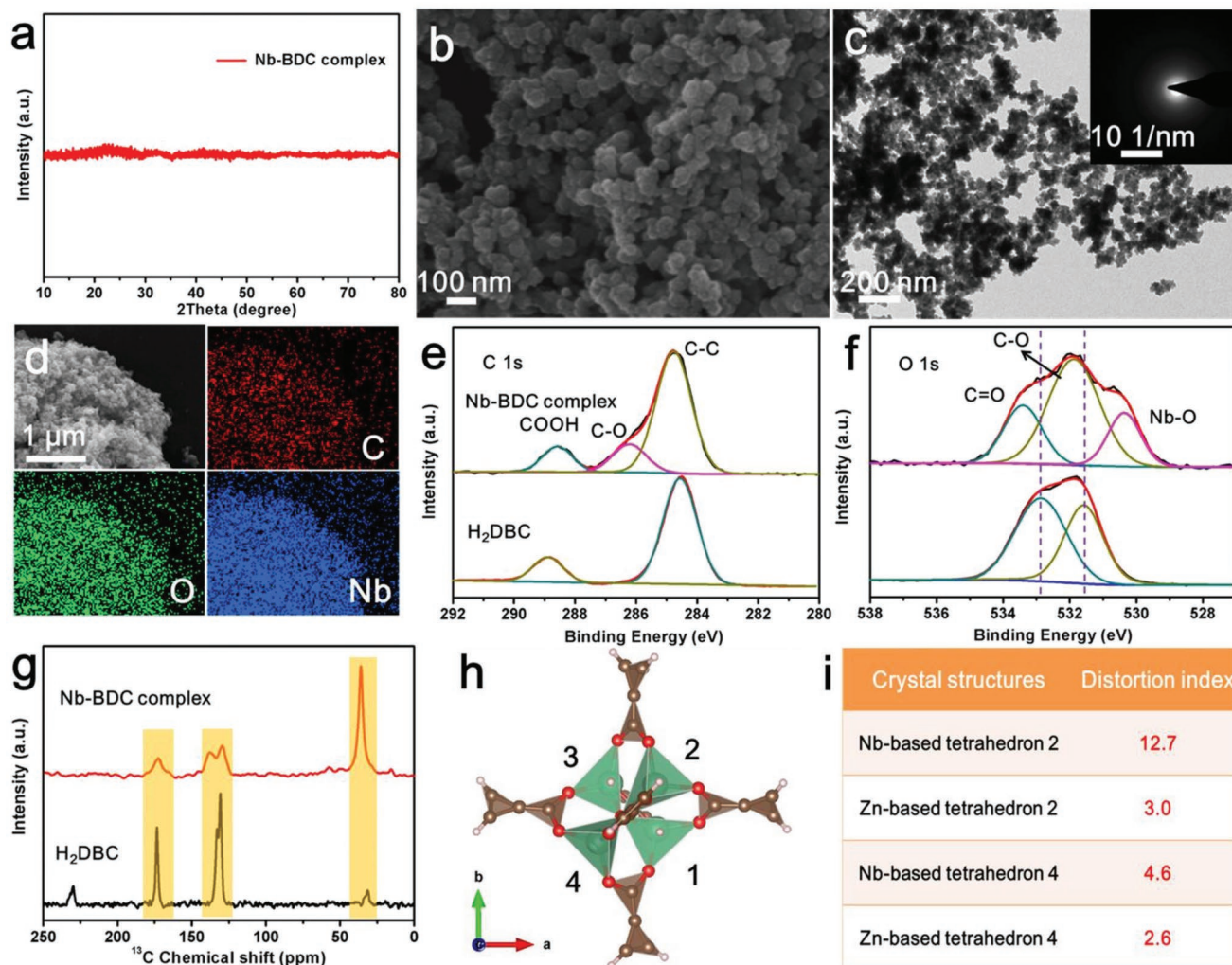


Figure 2. Characterizations of the Nb-BDC complex nanoparticles. a) XRD pattern. b) SEM image. c) TEM image. Inset of (c) is SAED pattern. d) EDX mapping image, including C, O, and Nb elements. e, f) High-resolution C 1s and O 1s XPS spectra of Nb-BDC complex and H₂BDC, respectively. g) ¹³C cross-polarization (CP) magic angle spinning (MAS) solid-state NMR spectra of Nb-BDC complex (red line) and terephthalic acid (black line), respectively. h) DFT calculations on the crystal structure of Nb-BDC complex by using Nb⁵⁺ to replace Zn²⁺ of Zn-MOF-5. i) Comparisons of crystal structures between Nb-BDC complex and Zn-MOF-5.

cell parameters of $a = 20.381$, $b = 3.825$, $c = 19.368$ Å, $\beta = 115.7^\circ$. Compared with both TT-Nb₂O₅ and T-Nb₂O₅, the crystal cell of H-Nb₂O₅ is composed of NbO₆ octahedral sharing corners or edges without the characteristic pentagonal bipyramid units.

The formation processes of these three typical carbon-confined Nb₂O₅ samples were illustrated in Figure S2 (Supporting Information). First, during the solvothermal process, the mismatched coordination reaction occurred between metal ions (Nb⁵⁺) and organic ligands (1,4-dicarboxybenzene, denoted as H₂BDC) because of their mismatched bonding angles and/or distorted metal-based polyhedra.^[18] Therefore, amorphous metal-ligand (Nb-BDC) complexes were formed, which were assembled by coordination bonds and intermolecular forces. A series of characterizations were carried out to reveal the structure of the obtained amorphous metal-ligand complexes (Figure 2). XRD pattern showed no obvious diffraction peaks, indicating its amorphous structure (Figure 2a). Field-emission scanning electron microscopy (SEM) and transmission electron microscopy (TEM)

images showed the obtained metal-ligand complex nanoparticles with the size of less than 100 nm (Figure 2b,c). The selected area electron diffraction (SAED) pattern displayed no diffraction rings, further confirming the amorphous product without long-range order (inset of Figure 2c). The energy-dispersive X-ray (EDX) elemental mapping images indicated a uniform distribution of the Nb, O, and C elements all over the selected area (Figure 2d). Fourier-Transform Infrared (FTIR) spectrum of the Nb-BDC complexes had some typical bond vibrations of H₂BDC, indicating the occurrence of the coordination reaction (Figure S3a, Supporting Information). The nitrogen adsorption-desorption isotherm of the Nb-BDC complexes showed a high Brunauer-Emmett-Teller (BET) specific surface area of 214.4 m² g⁻¹ (Figure S3b, Supporting Information). The pore size distribution was mainly below 2 nm, belonging to micropores (Figure S3c, Supporting Information). Furthermore, X-ray photoelectron spectroscopy (XPS) was performed to identify the bonding structure of the Nb-BDC complexes. XPS full spectrum

showed the existence of Nb, C, and O elements (Figure S3d, Supporting Information). High-resolution C 1s and O 1s XPS spectra demonstrated the newly formed C–O and Nb–O bonds existed in the Nb–BDC complexes, and the positive shift of C–O and C=O bonds indicated efficient electron transfer from the O atoms to Nb atoms, directly confirming the occurrence of mismatched coordination reaction (Figure 2e,f). Solid-state nuclear magnetic resonance (NMR) measurement was also carried out to reveal the structure of the amorphous Nb–BDC complexes (Figure 2g). All resonances in the ^{13}C cross-polarization (CP) magic angle spinning (MAS) NMR spectrum of the Nb–BDC complexes were much broader than those in crystalline 1,4-dicarboxybenzene, further confirming the amorphous structure of the Nb–BDC complexes. By using Nb^{5+} to replace Zn^{2+} of crystalline MOF-5, the local structure of the Nb–BDC complexes was illustrated after density functional theory (DFT) calculations (Figure 2h). The distortion indexes of the Nb-based tetrahedra (12.7 and 4.6) were higher than those of the Zn-based tetrahedra in MOF-5 (3.0 and 2.6) (Figure 2i). These distorted Nb-based polyhedra led to the formation of amorphous Nb–BDC complexes without long-range order. Therefore, this mismatched coordination reaction plays an important role in the small size of the Nb–BDC complexes.

In addition, the formation of carbon-confined Nb_2O_5 nanoparticles with different phases is highly determined by

subsequently controlled pyrolysis of the as-prepared Nb–BDC complex precursors. Thermal gravimetric (TG) analysis of the Nb–BDC complexes under argon condition showed a major mass loss of ≈ 14 wt% below 450°C and a small mass loss of ≈ 2.5 wt% above 800°C , which were attributed to the carbonization of organic ligands and the partial carbon oxidation, respectively (Figure S3f, Supporting Information). Systematic XRD measurement was carried out to investigate the structural evolution of the derived products upon heating the Nb–BDC complex precursor in hydrogen/argon (5%/95%) condition at different temperatures ranging from 400 to 1000°C (Figure S4, Supporting Information). The whole process included four major stages showing different structures as follows: first, the derived products were amorphous from 400 to 550°C ; second, pure TT- Nb_2O_5 phase was observed from 600 to 700°C ; third, pure T- Nb_2O_5 phase was found from 750 to 850°C ; finally, pure H- Nb_2O_5 phase was obtained from 900 to 1000°C . Therefore, by simply modulating different heat treatment of the as-prepared Nb–BDC complex precursors, three typical carbon-confined Nb_2O_5 nanoparticles were easily obtained.

A series of characterizations were carried out to reveal the structures of these three typical carbon-confined Nb_2O_5 nanoparticles (Figure 3; Figures S5–S8, Supporting Information). XRD patterns displayed their phases without any impurities

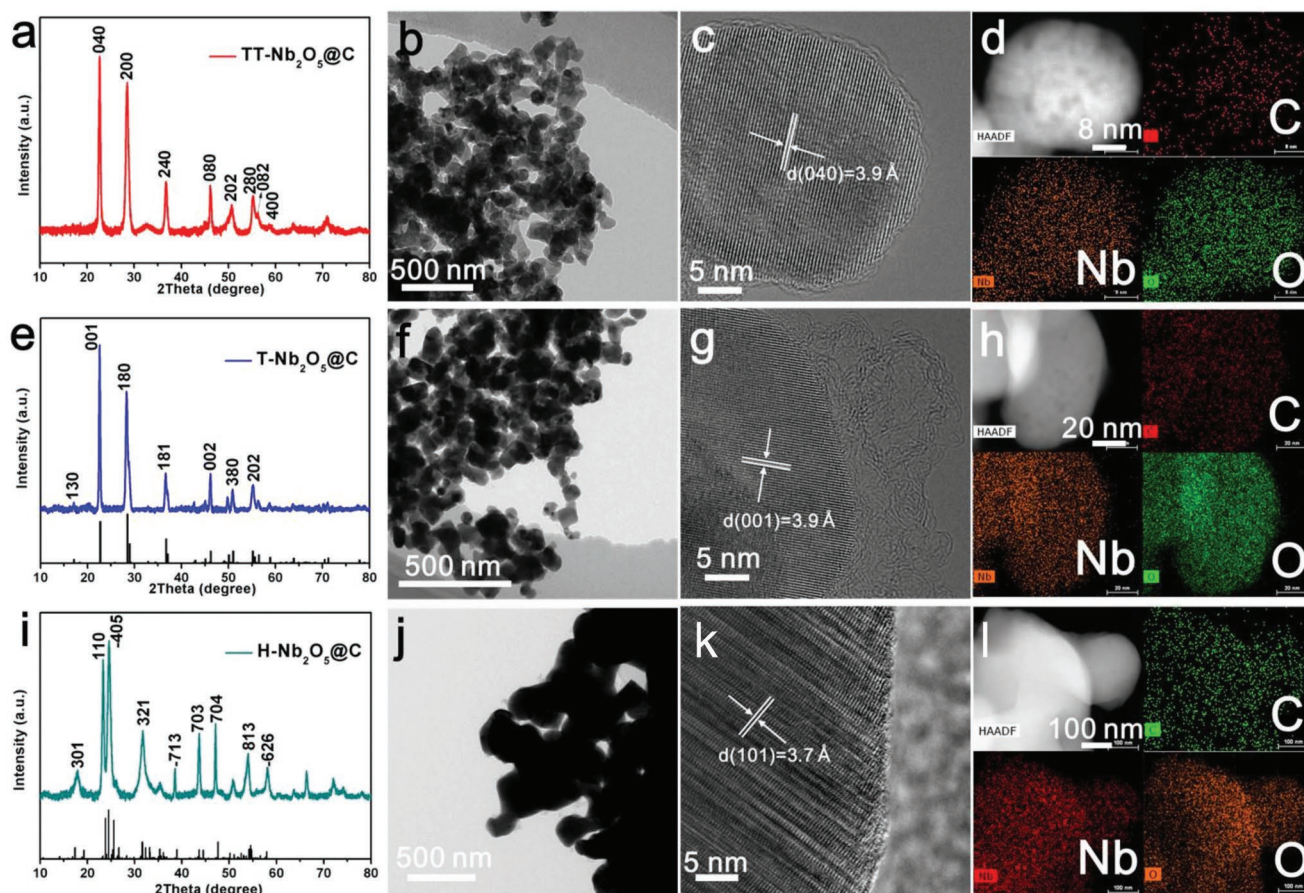


Figure 3. a) XRD pattern, b) TEM image, c) HRTEM image, d) HAADF-STEM image and EDS mapping images of TT- Nb_2O_5 @C nanoparticles. e) XRD pattern, f) TEM image, g) HRTEM image, h) HAADF-STEM image and EDS mapping images of T- Nb_2O_5 @C nanoparticles. i) XRD pattern, j) TEM image, k) HRTEM image, l) HAADF-STEM image and EDS mapping images of H- Nb_2O_5 @C nanoparticles.

(Figure 3a,e,i). TT-Nb₂O₅@C nanoparticles displayed the pseudo-hexagonal phase, which was in accordance with previous reports, while T-Nb₂O₅@C and H-Nb₂O₅@C nanoparticles displayed the orthorhombic and the monoclinic phases (JCPDS No. 00-027-1003 and JCPDS No. 00-037-1468), respectively.^[16,17] As shown in SEM and TEM images, three carbon-confined Nb₂O₅ nanoparticles possessed similar morphologies, which had many small nanoparticles with an average diameter of 100–300 nm (Figure 3b,f,j; Figure S5a–c, Supporting Information). The corresponding SEM energy-dispersive X-ray spectroscopy (EDS) mapping images displayed a uniform distribution of Nb, C, and O elements (Figure S5d–f, Supporting Information). Furthermore, high-resolution TEM images demonstrated single-crystalline nanoparticles with thin carbon coating (Figure 3c,g,k). The interlayer spacings of TT-Nb₂O₅@C, T-Nb₂O₅@C, and H-Nb₂O₅@C were calculated to be 3.9, 3.9, and 3.7 Å, which were well consistent with their typical lattice planes of (040), (001), and (101), respectively. The high-angle annular dark-field scanning-TEM (HAADF-STEM) images and the corresponding EDS mapping images further confirmed uniform distributions of Nb, O, and C elements all over selected nanoparticles (Figure 3d,h,l). Therefore, the thin carbon coating and nanoscale size can endow Nb₂O₅ with a high surface area, high conductivity, and short diffusion length, which are beneficial for ultrafast and stable lithium storage.

Raman spectra of these carbon-confined Nb₂O₅ nanoparticles showed characteristic bands (Figure S6a, Supporting Information). Two obvious bands located at ≈1350 and 1600 cm⁻¹ were attributed to the D band (disoriented carbon) and G band (graphitic carbon), respectively. The I_D/I_G ratios of TT-Nb₂O₅@C, T-Nb₂O₅@C, and H-Nb₂O₅@C were calculated to be 0.95, 1.01, and 1.09, indicating the partial graphitization degree of their carbon coatings. In addition, a high-wavenumber band group (ν_{Hi}) ranging from 570 to 770 cm⁻¹ and a mid-wavenumber band group (ν_{Mid}) ranging from 180 to 360 cm⁻¹ belonged to Nb₂O₅. FTIR spectra displayed similar and typical curves like inorganic materials (Figure S6b, Supporting Information). TG results showed that the mass contents of carbon were below 3 wt%, which may be beneficial for high energy density (Figure S6c, Supporting Information). The surface chemical bonding states of the carbon-confined Nb₂O₅ samples were investigated by XPS and electron paramagnetic resonance (EPR) measurements. XPS spectra demonstrated the existence of Nb, O, and C elements in three samples (Figure S6d, Supporting Information). From the high resolution Nb 3p XPS spectra, both Nb⁵⁺ and Nb⁴⁺ existed in them because of the surface reduction in high temperature condition (Figure S6e, Supporting Information). This phenomenon can result in the formation of oxygen vacancies on the surface. Bare Nb₂O₅ sample did not exhibit characteristic EPR response, while TT-Nb₂O₅@C, T-Nb₂O₅@C, and H-Nb₂O₅@C samples displayed the distinct EPR signals with *g* values of 1.97, 1.98, and 1.98, further indicating the existence of Nb⁴⁺ on their surfaces (Figure S6f, Supporting Information).^[19] Nitrogen adsorption–desorption analysis showed that the BET specific surface areas of TT-Nb₂O₅@C, T-Nb₂O₅@C, and H-Nb₂O₅@C were around 45.5, 42.7, and 36.4 m² g⁻¹, respectively (Figure S7, Supporting Information). The decreased specific surface areas from TT-Nb₂O₅@C to H-Nb₂O₅@C were owing to their increased

temperature treatment. The pore size distribution of them was below 5 nm, which was mainly attributed to the random stacking of nanoparticles.

Furthermore, to identify their structure–property relationships, the electrochemical performances of the as-prepared TT-Nb₂O₅@C, T-Nb₂O₅@C, and H-Nb₂O₅@C samples were employed as anode materials for LIBs (Figure 4). First, the cyclic voltammetry (CV) measurements were carried out in a potential range from 1.1 to 3.0 V versus Li⁺/Li at a scan rate of 0.2 mV s⁻¹ (Figure 4a–c). The first six CV curves of TT-Nb₂O₅@C and T-Nb₂O₅@C were similar and displayed relatively broad reversible peaks, which were attributed to their similar open frameworks. In detail, a broad anodic peak at 1.86 V and two broad cathodic peaks at 1.41 and 1.78 V were observed in TT-Nb₂O₅@C, and T-Nb₂O₅@C had two broad anodic peaks at 1.82 and 2.08 V and two broad cathodic peaks at 1.55 and 1.80 V. However, H-Nb₂O₅@C showed sharp reversible peaks of CV curves with a major pair at 1.73/1.62 V and two small pairs at 1.26/1.17 V and 2.10/2.0 V. This difference among them was highly dependent by their crystal structures. The main cathodic and anodic peaks corresponded to Li insertion/extraction to/from the Nb₂O₅ lattices. The peak currents from TT-Nb₂O₅@C to H-Nb₂O₅@C were increased, indicating that H-Nb₂O₅@C displayed higher specific capacity compared to the other polymorphs. The charge–discharge curves of TT-Nb₂O₅@C, T-Nb₂O₅@C, and H-Nb₂O₅@C samples at different rates were also performed (Figure 4d–f). TT-Nb₂O₅@C and T-Nb₂O₅@C displayed smooth sloping voltage curves, while H-Nb₂O₅@C showed an obvious platform, which was in consistence with the observations in CV curves. When tested at a low current density of 0.1 A g⁻¹, H-Nb₂O₅@C possessed a higher discharge capacity of 230.7 mAh g⁻¹ than TT-Nb₂O₅@C and T-Nb₂O₅@C (187.1 and 205.2 mAh g⁻¹), indicating more lithium storage sites in H-Nb₂O₅. However, when tested at a high current density of 6 A g⁻¹, T-Nb₂O₅@C exhibited a higher discharge capacity of 177.3 mAh g⁻¹ compared to TT-Nb₂O₅@C and H-Nb₂O₅@C (129.2 and 136.5 mAh g⁻¹). The corresponding capacity retentions of TT-Nb₂O₅@C, T-Nb₂O₅@C, and H-Nb₂O₅@C at 0.1 A g⁻¹ were 69.1%, 86.4%, and 59.2%, respectively, indicating excellent rate capability in T-Nb₂O₅. Moreover, after 200 cycles at 0.2 A g⁻¹, T-Nb₂O₅@C sample exhibited a higher discharge capacity of 181.3 mAh g⁻¹ and a higher capacity retention of 92.2% than those of TT-Nb₂O₅@C (153.4 mAh g⁻¹, 90.2%) and H-Nb₂O₅@C (179.3 mAh g⁻¹, 78.1%), confirming its excellent cycling stability (Figure 4g). The corresponding Coulombic efficiencies of these three samples were shown in Figure S8 (Supporting Information). The rate performance was measured at various current densities ranging from 0.1 to 6 A g⁻¹ (Figure 4h). T-Nb₂O₅@C among three samples possessed superior rate capability. Highly reversible average discharge capacities of 204.7, 198.6, 193.2, 189.7, 184.9, 183.5, 181.6, 178.8, and 177.2 mAh g⁻¹ were obtained at 0.1, 0.2, 0.5, 1, 2, 3, 4, 5, and 6 A g⁻¹, respectively. The corresponding charge/discharge curves at different current densities were shown in Figure 4d–f, indicating ultrafast lithium storage and low overpotential. When returned to 0.1 A g⁻¹, the specific discharge capacity of 197.5 mAh g⁻¹ was obtained, corresponding to a high capacity retention of 98.5%. Furthermore, when tested at

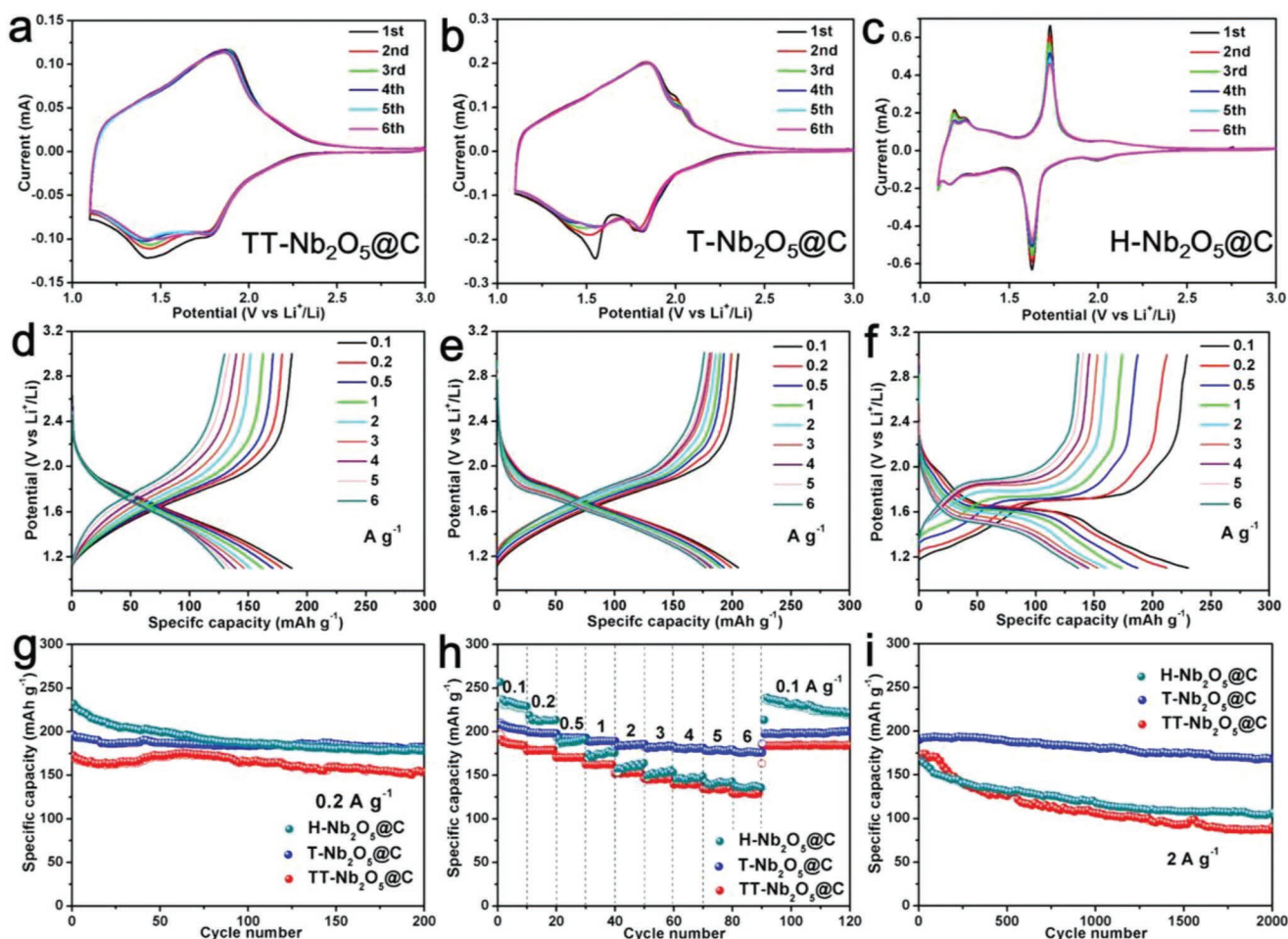


Figure 4. Lithium storage performances of the obtained TT-Nb₂O₅@C, T-Nb₂O₅@C, and H-Nb₂O₅@C samples. a–c) The first six CV curves for TT-Nb₂O₅@C, T-Nb₂O₅@C, and H-Nb₂O₅@C samples tested at a scan rate of 0.2 mV s⁻¹, respectively. d–f) Charge–discharge curves at different current densities of TT-Nb₂O₅@C, T-Nb₂O₅@C, and H-Nb₂O₅@C samples, respectively. g) Cycling performances tested at a low current density of 0.2 A g⁻¹. h) Rate performances tested at various current densities ranging from 0.1, 0.2, 0.5, 1, 2, 3, 4, 5, and 6, back to 0.1 A g⁻¹. i) Cycling performances tested at a high current density of 2 A g⁻¹.

a high current density of 2 A g⁻¹ after 2000 cycles, T-Nb₂O₅@C sample possessed a higher specific discharge capacity of 169.6 mAh g⁻¹ and a higher capacity retention of 87.9% than those of TT-Nb₂O₅@C (88.5 mAh g⁻¹, 51.9%) and H-Nb₂O₅@C (105.5 mAh g⁻¹, 63.1%) (Figure 4i). Therefore, T-Nb₂O₅@C displayed ultrafast lithium storage and outstanding long-term cycling stability, which showed great potential for ultrafast LIBs.

Furthermore, to understand the superior performance of T-Nb₂O₅@C, CV measurement was carried out to evaluate its electrochemical kinetics (Figure S9a,b, Supporting Information). The CV curves at various scan rates from 0.1 to 20 mV s⁻¹ displayed similar broad peaks and small polarization. In previous reports, the relationship between measured currents (*i*) and scan rates (*v*) was described as follows: $i = av^b$.^[20] After transformation of this equation, the *b* value was highly dependent on the slope value of the log(*i*)–log(*v*) plots (Figure S9c, Supporting Information). The *b* values for both cathodic and anodic peaks were calculated to be about 0.99 at scan rates from 0.1 to 20 mV s⁻¹, which was in accordance with the observations from Dunn and co-workers.^[9] This phenomenon indicated

that T-Nb₂O₅@C possessed ultrafast and surface-controlled kinetics with typical capacitive characteristics. Furthermore, electrochemical impedance spectroscopy was performed to evaluate the charge-transfer resistances (*R*_{ct}) and the lithium ion diffusion kinetics of these different electrodes. The *R*_{ct} value of T-Nb₂O₅@C was ≈26.7 Ω, which was smaller than those of TT-Nb₂O₅@C (41.2 Ω), H-Nb₂O₅@C (101.5 Ω), and pure T-Nb₂O₅ (37.2 Ω), indicating fast electronic mobility (Figures S9d and S10a, Supporting Information). From the kinetics calculation based on the frequency ($\omega^{-1/2}$) and *Z'* values in low frequency region, T-Nb₂O₅@C exhibits the lowest slope value of 25.7 compared with TT-Nb₂O₅@C (28.6) and H-Nb₂O₅@C (80.8) (Figure S10b, Supporting Information). The slope value is defined as Warburg factor and its square values have an inverse relationship with lithium ion diffusion coefficient.^[21] By contrast, the T-Nb₂O₅@C displayed the fastest diffusion kinetics among them. In addition, galvanostatic intermittent titration technique (GITT) was further carried out to compare the Li-ion diffusion kinetics of TT-Nb₂O₅@C, T-Nb₂O₅@C, and H-Nb₂O₅@C at nearly thermodynamic equilibrium conditions.

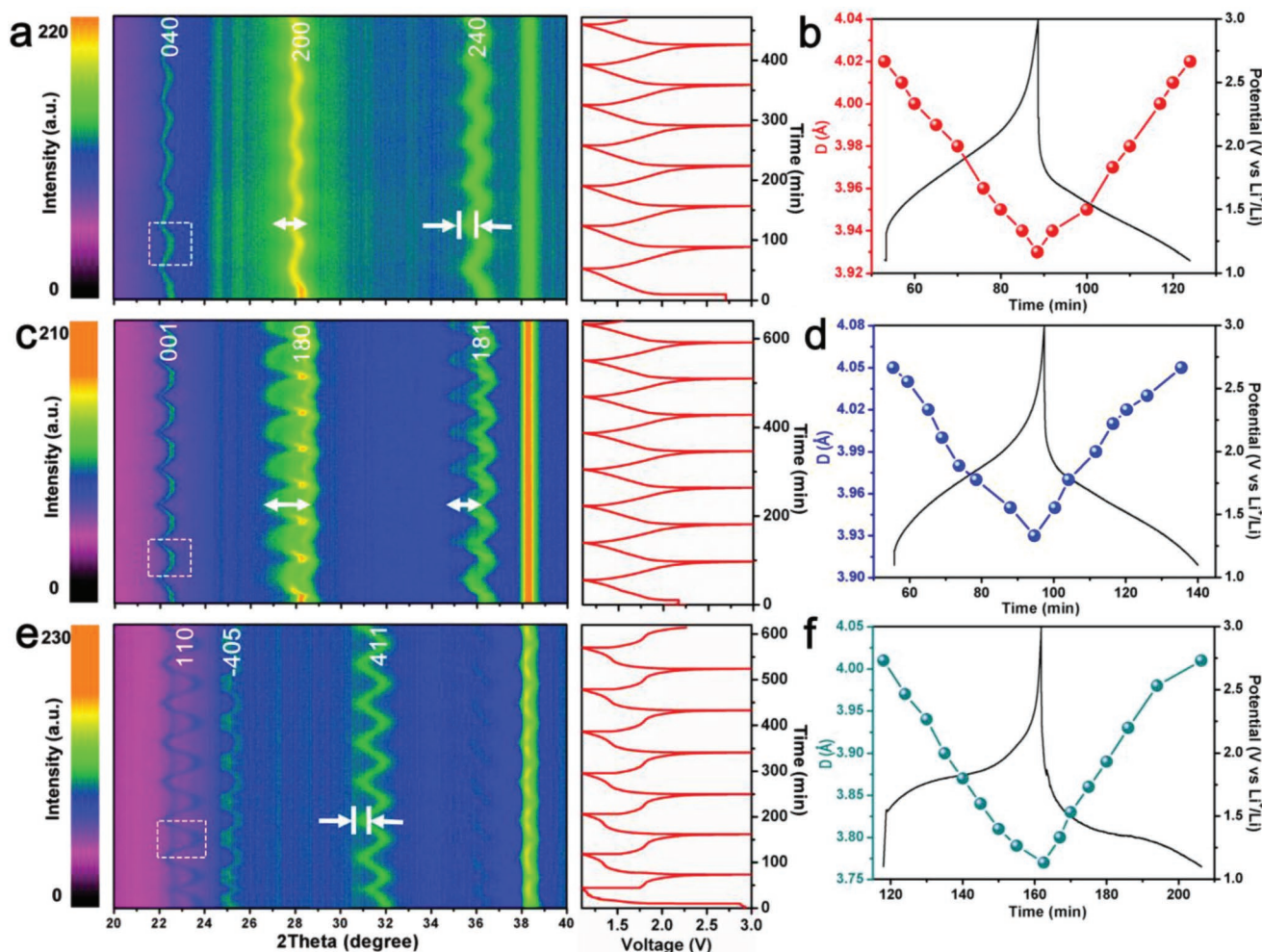


Figure 5. In situ XRD patterns of a) TT-Nb₂O₅@C, c) T-Nb₂O₅@C, e) and H-Nb₂O₅@C samples during galvanostatic charge and discharge at 0.2 A g⁻¹. The horizontal axis represents the selected 2θ regions from 20°–40°, and time is plotted on the vertical axis. The corresponding voltage curves plotted to the right. The diffraction intensity is color-coded according to the scale bar in the left. The interlayer spacing (*D*) evolution of b) (040) plane in TT-Nb₂O₅@C, d) (001) plane in T-Nb₂O₅@C, and f) (110) plane in H-Nb₂O₅@C samples during galvanostatic charge and discharge at 0.2 A g⁻¹.

To obtain a quasi-steady state, GITT data were collected at a current density of 50 mA g⁻¹ and a time interval of 30 min in the potential range from 1.1 to 3.0 V (Figure S11, Supporting Information). On basis of the reported simplified formula, the square value of the ratio of the average steady voltage difference (ΔE_s) and voltage drop (ΔE_t) has a linear relationship with lithium ion diffusion coefficient.^[22] During the charge process, the ratio of ΔE_s and ΔE_t in T-Nb₂O₅@C near the average voltage is 0.81 and much larger than those in TT-Nb₂O₅@C (0.51) and H-Nb₂O₅@C (0.36), qualitatively confirming the highest diffusion coefficient of T-Nb₂O₅@C.

To better reveal the lithium storage mechanisms of TT-Nb₂O₅@C, T-Nb₂O₅@C, and H-Nb₂O₅@C, time-resolved in situ XRD technique was carried out to investigate their structural evolution during the charge and discharge processes.^[23] The clear and high-quality XRD patterns were obtained during several original cycles of galvanostatic lithium insertion/extraction processes at 0.2 A g⁻¹ in the potential range of 1.1–3.0 V (Figure 5). Major diffraction peaks of them were covered in the selected 2θ region of 20°–40°. At the open circuit voltage

state, all the diffraction peaks were assigned to pure phases. For T-Nb₂O₅@C, the diffraction peaks located at 22.6°, 28.3°, and 36.5° correspond to the (001), (180), and (181) planes, respectively. TT-Nb₂O₅@C exhibited similar three diffraction peaks compared to those in T-Nb₂O₅@C, corresponding to (040), (200), and (240) planes, respectively. For H-Nb₂O₅@C, three major diffraction peaks centered at 24.4°, 25.5°, and 32.2° were observed, corresponding to the (110), (−405), and (411) planes, respectively.

These in situ XRD patterns displayed three main characteristics of their diffraction peaks during the lithium insertion/extraction processes. First, when discharging, all the positions of these typical diffraction peaks gradually shifted to low angles. It indicated that the lattice spacings of their corresponding planes expanded with the intercalation of Li⁺, along with the formation of Li_xNb₂O₅. This phenomenon was attributed to the formation of larger Nb⁴⁺ cations (ionic radius: 0.83 Å) compared to Nb⁵⁺ cations (0.78 Å). Conversely, during charging, these diffraction peaks reversibly recovered and gradually shifted to high angles because of the lithium extraction from

$\text{Li}_x\text{Nb}_2\text{O}_5$. The continuous variation of these typical diffraction peaks without the existence of new diffraction peaks confirmed that the lithium storage mechanisms of $\text{TT-Nb}_2\text{O}_5@\text{C}$, $\text{T-Nb}_2\text{O}_5@\text{C}$, and $\text{H-Nb}_2\text{O}_5@\text{C}$ were one-phase solid solution reactions.^[6a] Because of no phase transformations, the solid solution reaction was beneficial for fast lithium storage in electrode materials. Second, the specific capacity and cycling stability of the electrode materials were highly determined by the variation of the interlayer spacings of typical diffraction planes. The major planes of $\text{TT-Nb}_2\text{O}_5@\text{C}$, $\text{T-Nb}_2\text{O}_5@\text{C}$, and $\text{H-Nb}_2\text{O}_5@\text{C}$ were (040), (001), and (110), respectively. Based on the Bragg equation, the interlayer spacing of (040) plane in $\text{TT-Nb}_2\text{O}_5@\text{C}$ changed from 3.93 to 4.02 Å, corresponding to the increment rate of $\approx 2.29\%$; for $\text{T-Nb}_2\text{O}_5@\text{C}$, the variation of the interlayer spacing of (001) plane was from 3.93 to 4.05 Å, corresponding to the increment rate of $\approx 3.05\%$. Compared to $\text{TT-Nb}_2\text{O}_5@\text{C}$, $\text{T-Nb}_2\text{O}_5@\text{C}$ exhibited larger increment rate, indicating more lithium storage sites and thus higher specific capacity. In addition, the in situ XRD patterns of $\text{TT-Nb}_2\text{O}_5@\text{C}$ showed the peak intensity of the (200) plane decreased along with the cycling process, indicating its decreased crystallinity (Figure 5a). Conversely, $\text{T-Nb}_2\text{O}_5@\text{C}$ displayed good structural stability (Figure 5c). These phenomena further explained the reason on the worse cycling stability of $\text{TT-Nb}_2\text{O}_5@\text{C}$. For $\text{H-Nb}_2\text{O}_5@\text{C}$, the interlayer spacing of (110) plane varied from 3.77 to 4.01 Å, and the corresponding increment rate was about 6.37%, much higher than those of $\text{TT-Nb}_2\text{O}_5@\text{C}$ and $\text{T-Nb}_2\text{O}_5@\text{C}$ (2.29% and 3.05%) (Figure 5b,d,f). This large variation endowed $\text{H-Nb}_2\text{O}_5@\text{C}$ with high specific capacity but led to major structural distortion and thus poor cycling stability. Third, $\text{T-Nb}_2\text{O}_5@\text{C}$ showed two broad diffraction peaks indexed as (810) and (811) planes upon cycling. In the views from *a*-axis and *c*-axis, the (810) and (811) planes came from layer internal configuration of $\text{T-Nb}_2\text{O}_5@\text{C}$, which was assembled with NbO_6 and NbO_7 polyhedra by sharing their corners and/or edges (Figure 1b; Figure S12, Supporting Information). When Li^+ was inserted into the interlayer spacings during discharging, the valence state of partial Nb atoms in $\text{T-Nb}_2\text{O}_5$ varied from +5 to +4, resulting in the volume increase of NbO_6 and NbO_7 polyhedra and thus the shift to low diffraction angle of typical (810) and (811) planes. As shown in time-resolved in situ XRD patterns, the broad dispersive diffraction peaks indicated that the continuous and random insertion of lithium on the layer surface configurations occurred without any barrier limitations from crystal lattices. This phenomenon was attributed to a quasi-2D network for Li-ion transport in $\text{T-Nb}_2\text{O}_5@\text{C}$, further confirming ultrafast lithium storage. However, for $\text{H-Nb}_2\text{O}_5@\text{C}$, the narrow diffraction peaks of (-405) and (411) planes were observed, indicating the limited transport pathway of lithium in its crystal lattices. It led to relatively poor rate capability, which was confirmed by the abovementioned electrochemical tests. To sum up, the advanced in situ XRD technique demonstrated that the solid solution reaction mechanism, appropriate variation of interlayer spacings, and ultrafast lithium transports endowed the $\text{T-Nb}_2\text{O}_5@\text{C}$ with high rate performance and long-life cycling stability.

To further explain the experimental results and identify different kinetics of Li-ion diffusion among $\text{TT-Nb}_2\text{O}_5$, $\text{T-Nb}_2\text{O}_5$, and $\text{H-Nb}_2\text{O}_5$, a series of DFT calculations were performed to

investigate the detailed information of their migration paths and migration energy during Li insertion process (Figure 6). Due to their solid solution reaction mechanisms, Li-diffusion pathways involve conventional vacancy hopping between all neighboring Li positions along each of the diffusion channels in crystal lattices.^[24] As relatively looser packed layers and tunnels are believed to have less hindrance for Li ions transport, we simulate the most feasible migration paths for Li ions in $\text{TT-Nb}_2\text{O}_5$, $\text{T-Nb}_2\text{O}_5$, and $\text{H-Nb}_2\text{O}_5$.^[7b] In view of *ac*-plane and *ab*-plane, the Li migration pathway of $\text{TT-Nb}_2\text{O}_5$ is parallel to the *a*- and *b*-axes with a zigzagged trajectory (Figure 6a,b). Similarly, in view of *bc*-plane and *ab*-plane, the Li migration pathway of $\text{T-Nb}_2\text{O}_5$ is parallel to the *a*- and *b*-axes with an armchair trajectory (Figure 6d,e). These results indicate high Li^+ mobility within the *ab* plane, confirming quasi-2D Li migration in both $\text{TT-Nb}_2\text{O}_5$ and $\text{T-Nb}_2\text{O}_5$. However, our calculations reveal that $\text{H-Nb}_2\text{O}_5$ exhibits 3D curved paths for long-range Li migration, displaying relatively slow Li diffusion kinetics (Figure 6g,h). The corresponding energy profiles for Li migration along each of these paths can be calculated out. During the Li migration process, the highest migration energy is the rate-determined step for Li diffusion coefficient. By contrast, the highest migration energy values of $\text{TT-Nb}_2\text{O}_5$, $\text{T-Nb}_2\text{O}_5$, and $\text{H-Nb}_2\text{O}_5$ are 0.46, 0.47, and 1.14 eV, respectively (Figure 6c,f,i). Considering the influence of error which is introduced in the estimation of diffusion coefficient from the migration energy, the difference between diffusion coefficients of $\text{TT-Nb}_2\text{O}_5$ and $\text{T-Nb}_2\text{O}_5$ should be actually indistinguishable. Therefore, our calculation proposes that the Li diffusion coefficients are ordered in the sequence of $\text{TT-Nb}_2\text{O}_5 \approx \text{T-Nb}_2\text{O}_5 \gg \text{H-Nb}_2\text{O}_5$. Furthermore, the Li diffusion flux plays an important role on the rate performance for Li storage. The local rule for diffusion flux *J* is given by Fick's 1st law of diffusion

$$J = -D \frac{dc}{dx} \quad (1)$$

in which the flux *J* [$\text{cm}^{-2} \text{s}^{-1}$] is proportional to the diffusivity *D* [$\text{cm}^2 \text{s}^{-1}$] and the negative gradient of concentration, $\frac{dc}{dx}$ [$\text{cm}^{-3} \text{cm}^{-1}$]. Thus, a long diffusion distance corresponds to the gradient of concentration, resulting in a small diffusion flux *J*. From our calculations, the diffusion distance in $\text{T-Nb}_2\text{O}_5$ is 2.26 Å, which is shorter than that of $\text{TT-Nb}_2\text{O}_5$ (4.40 Å). Considering their similar diffusion coefficient *D*, the diffusion flux *J* in $\text{T-Nb}_2\text{O}_5$ will be higher than that in $\text{TT-Nb}_2\text{O}_5$. In addition, the longer diffusion distance for $\text{TT-Nb}_2\text{O}_5$ costs more time to complete the diffusion. Therefore, the $\text{T-Nb}_2\text{O}_5$ exhibits highest diffusion flux compared with $\text{TT-Nb}_2\text{O}_5$ and $\text{H-Nb}_2\text{O}_5$, showing the best rate performance.

Because of the relatively small differences among the Li migration energies (less than 0.2 eV), the incorporated Li^+ can be efficiently located in all storage sites of $\text{T-Nb}_2\text{O}_5$ and $\text{TT-Nb}_2\text{O}_5$. Further, this phenomenon results in the formation of smooth sloping capacity–voltage curves during the Li^+ insertion/extraction process, which is in accordance with the experimental observations. Conversely, the large difference among the Li migration energies with about 1.0 eV indicates the fixed locations for Li storage, thus corresponding to a clear voltage platform during the electrochemical process. Furthermore, the detailed Li^+ migration states at the

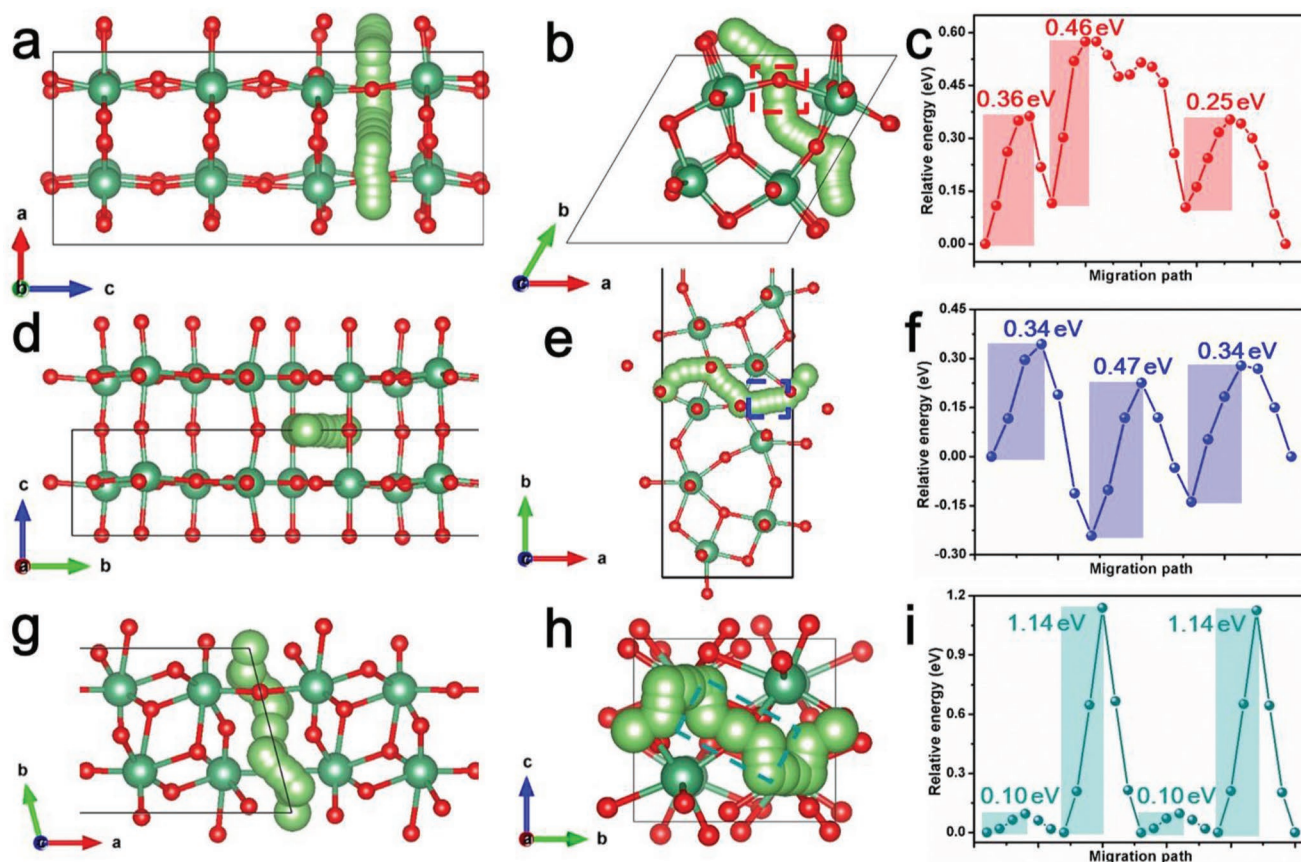


Figure 6. Simulated Li^+ migration paths viewed from different lattice planes of a,b) $\text{TT-Nb}_2\text{O}_5$, d,e) $\text{T-Nb}_2\text{O}_5$, g,h) $\text{H-Nb}_2\text{O}_5$, and c,f,i) their respective corresponding migration energy profiles. The rectangular boxes represent the Li^+ migration regions near the highest energy barrier.

highest migration energy were analyzed to reveal the origin of different energy barriers in $\text{TT-Nb}_2\text{O}_5$, $\text{T-Nb}_2\text{O}_5$, and $\text{H-Nb}_2\text{O}_5$ (Figures S13–S15, Supporting Information). The Li atoms in $\text{TT-Nb}_2\text{O}_5$, $\text{T-Nb}_2\text{O}_5$, and $\text{H-Nb}_2\text{O}_5$ coordinated with oxygen atoms by LiO_4 , LiO_6 , and LiO_4 structures, respectively. The shortest bond length in $\text{H-Nb}_2\text{O}_5$ was about 1.74 Å, smaller than that in $\text{TT-Nb}_2\text{O}_5$ (1.90 Å) and $\text{T-Nb}_2\text{O}_5$ (1.84 Å), corresponding to larger bonding energy between Li and O atoms. Therefore, the relatively narrow diffusion channels and strong bonding energy with oxygen in $\text{H-Nb}_2\text{O}_5$ directly led to high-hindrance migration of Li ions.

3. Conclusions

In summary, we designed and constructed three typical carbon-confined Nb_2O_5 ($\text{TT-Nb}_2\text{O}_5@C$, $\text{T-Nb}_2\text{O}_5@C$, and $\text{H-Nb}_2\text{O}_5@C$) nanoparticles by a facile and well-designed method. We have clearly shown that the mismatched coordination reaction results in the formation of amorphous metal–ligand complex precursor nanoparticles. The obtained carbon-confined Nb_2O_5 nanoparticles possessed high surface area, high conductivity, short electron/ion transport length, which greatly improved their electrochemical performance. Furthermore, we also systematically investigate different phase effects on their lithium storage properties based on both experimental and computational approaches.

When employed as LIB anode materials, the $\text{T-Nb}_2\text{O}_5@C$ nanoparticles display higher rate capability and better cycling stability compared to $\text{TT-Nb}_2\text{O}_5@C$ and $\text{H-Nb}_2\text{O}_5@C$. Even at 2 A g^{-1} after 2000 cycles, the $\text{T-Nb}_2\text{O}_5@C$ exhibited a higher specific discharge capacity of 169.6 mAh g^{-1} and a higher capacity retention of 87.9% than those of $\text{TT-Nb}_2\text{O}_5@C$ (88.5 mAh g^{-1} , 51.9%) and $\text{H-Nb}_2\text{O}_5@C$ (105.5 mAh g^{-1} , 63.1%). Systematic in situ XRD analysis and theoretical calculations revealed the lithium storage mechanisms and different Li-ion diffusion kinetics of $\text{TT-Nb}_2\text{O}_5$, $\text{T-Nb}_2\text{O}_5$, and $\text{H-Nb}_2\text{O}_5$. Our proposed insights can provide better guidance for the rational design of Nb_2O_5 structures for many frontier energy-related applications.

4. Experimental Section

Materials Synthesis: First, ≈ 200 mg of niobium pentachloride (NbCl_5) and 1 g of terephthalic acid (H_2BDC) were dissolved in 80 mL of N,N -dimethylformamide to obtain a transparent mixture after stirring 30 min. Then, the solution was transferred into a 100 mL Teflon-autoclave and allowed to stand for 12 h in an oven with the temperature of 200 °C. After the autoclave was naturally cooled down to room temperature, the interior mixture was centrifuged to obtain the precipitate, which was subsequently washed with ethanol for 3 times and then dried for 12 h in an oven at 70 °C. The dried white powder, Nb–BDC complex, was calcined for 3 h at set temperatures in hydrogen/argon (5%/95%) condition. The heating process was operated with a heating rate of 5 °C min^{-1} and a programmed temperature range of 400–1000 °C.

Finally, different carbon-confined Nb₂O₅ nanoparticles were obtained. In addition, when the Nb–BDC complex nanoparticles were treated at 700 °C for 3 h in air, T-Nb₂O₅ nanoparticles were obtained.

Characterizations: The crystallographic characteristics of the final products were measured using a Bruker D8 Discover X-ray diffractometer equipped with a Cu K α radiation source. SEM images were collected using a JEOL-7100F scanning electron microscope, and TEM images were collected using a JEM-2100F/Titan G2 60–300 transmission electron microscope. Energy-dispersive X-ray spectra were recorded using an Oxford IE250 system. Raman spectra were obtained using a Renishaw INVIA micro-Raman spectroscopy system. The BET surface area was calculated from nitrogen adsorption isotherms collected at 77 K using a Tristar-3020 instrument. XPS measurement was conducted using an ESCALAB 250Xi instrument. All solid-state NMR measurements were carried out on a 9.4 T Bruker Advance III HD NMR spectrometer equipped with a 4 mm HXY triple-resonance MAS probe at 1H Larmor frequency of 400.13 MHz with the X and Y channels tuned to ¹³C at 100.63 MHz. All NMR spectra were obtained with CP at MAS frequencies of 12 kHz for ¹³C. The EPR measurement was conducted with a Bruker EMX Plus spectrometer using an X band (9.78 GHz) at room temperature. For in situ XRD measurement, the electrode was placed right behind an X-ray-transparent beryllium window, which also acted as a current collector. The in situ XRD signals were collected using the planar detector in a still mode during the discharge–charge process, and each pattern took 2 min to acquire.

DFT Calculations: The present calculations are carried out by using the projector-augmented wave representations within the spin-polarized DFT as implemented in the Vienna Ab initio Simulation Package.^[25] The Perdew–Burke–Ernzerhof generalized-gradient approximation functional was used for all structural relaxations.^[26] The wave functions are expanded by using the plane waves up to a kinetic energy cutoff of 520 eV. Brillouin-zone integrations are approximated by using special k-point sampling of MonkhorstPack scheme with a k-point mesh resolution of $2\pi \times 0.05 \text{ \AA}^{-1}$.^[27] The unit cell lattice vectors (both the unit cell shape and size) are fully relaxed together with the atomic coordinates until the force on each atom is less than 0.01 eV \AA^{-1} and the energy convergence criterion is set to 1E–05 eV. Activation barrier calculations are performed with the climbing nudged elastic band (NEB) method in unit cells containing 8 f.u. (formula unit) for TT-Nb₂O₅ and 16 f.u. for H/T-Nb₂O₅.^[28] The large supercell isolates the hopping of atoms to their periodic images, providing an accurate way for calculating the activation barrier in the dilute limit (here, the images of the migrating Li are about 8 Å apart, which has been proved to be large enough to accurately estimate the activation barrier).^[29] During the NEB calculations, all the lattice parameters are fixed at the relaxed values of the fully delithiated structures, with all the internal degrees of freedom relaxed. The Bader analysis was performed using the Bader Charge Analysis Code.^[30]

Lithium Storage Measurements: The electrodes were composed of 80 wt% active materials, 10 wt% acetylene black, and 10 wt% carboxymethyl cellulose binder, forming a stable homogenous ink. After coating onto aluminum foil, the electrode film was uniformly cut into $\approx 0.5 \text{ cm}^2$ (area) round slices, weighing a total of $\approx 2.0 \text{ mg}$; the corresponding areal mass loading was 4.0 mg cm^{-2} . 2016 coin cells were assembled in a glovebox filled with pure argon gas. Lithium foil was used as the counter electrode and the separator was Celgard 2400 microporous membrane. 1 M lithium hexafluorophosphate (LiPF₆) solution in ethylene carbon–dimethyl carbonate (1:1 v/v) was used as the electrolyte. The amount of electrolyte in a cell is about 100 μL . Galvanostatic charge–discharge measurements were performed using a multichannel battery testing system (LAND CT2001A). CVs and electrochemical impedance spectra were collected at room temperature using an Autolab potentiostat/galvanostat.

Supporting Information

Supporting Information is available from the Wiley Online Library or from the author.

Acknowledgements

J.M., Q.H., and L.X. contributed equally to this work. This work was supported by the National Natural Science Fund for Distinguished Young Scholars (Grant No. 51425204), the National Natural Science Foundation of China (Grant Nos. 51832004, 51521001, and 51302203), the National Key Research and Development Program of China (Grant No. 2016YFA0202603), the Programme of Introducing Talents of Discipline to Universities (Grant No. B17034), the Yellow Crane Talent (Science & Technology) Program of Wuhan City, and the Fundamental Research Funds for the Central Universities (Grant Nos. WUT: 2016III001 and 2017III040).

Conflict of Interest

The authors declare no conflict of interest.

Keywords

carbon-confined Nb₂O₅, in situ XRD, lithium storage, phase control, theoretical calculation

Received: August 29, 2018

Revised: February 21, 2019

Published online:

- [1] a) Z. Yang, J. Zhang, M. C. Kintner-Meyer, X. Lu, D. Choi, J. P. Lemmon, J. Liu, *Chem. Rev.* **2011**, *111*, 3577; b) M. Armand, J. M. Tarascon, *Nature* **2008**, *451*, 652; c) A. Konarov, S.-T. Myung, Y.-K. Sun, *ACS Energy Lett.* **2017**, *2*, 703; d) X. Lin, Y. Liang, Z. Lu, H. Lou, X. Zhang, S. Liu, B. Zheng, R. Liu, R. Fu, D. Wu, *ACS Sustainable Chem. Eng.* **2017**, *5*, 8535; e) K. Leng, W. Mai, X. Zhang, R. Liu, X. Lin, J. Huang, H. Lou, Y. Xie, R. Fu, D. Wu, *Chem. Commun.* **2018**, *54*, 7159.
- [2] P. Simon, Y. Gogotsi, B. Dunn, *Science* **2014**, *343*, 1210.
- [3] a) N. S. Choi, Z. Chen, S. A. Freunberger, X. Ji, Y. K. Sun, K. Amine, G. Yushin, L. F. Nazar, J. Cho, P. G. Bruce, *Angew. Chem., Int. Ed.* **2012**, *51*, 9994; b) Y. Gogotsi, R. M. Penner, *ACS Nano* **2018**, *12*, 2081; c) L. Yu, L. Hu, B. Anasori, Y.-T. Liu, Q. Zhu, P. Zhang, Y. Gogotsi, B. Xu, *ACS Energy Lett.* **2018**, *3*, 1597.
- [4] Y. Tang, Y. Zhang, W. Li, B. Ma, X. Chen, *Chem. Soc. Rev.* **2015**, *44*, 5926.
- [5] a) F. Cheng, J. Liang, Z. Tao, J. Chen, *Adv. Mater.* **2011**, *23*, 1695; b) J. Meng, H. Guo, C. Niu, Y. Zhao, L. Xu, Q. Li, L. Mai, *Joule* **2017**, *1*, 522; c) J. B. Goodenough, Y. Kim, *Chem. Mater.* **2010**, *22*, 587; d) T. Yuan, Z. Tan, C. Ma, J. Yang, Z.-F. Ma, S. Zheng, *Adv. Energy Mater.* **2017**, *7*, 1601625.
- [6] a) A. Van der Ven, J. Bhattacharya, A. A. Belak, *Acc. Chem. Res.* **2013**, *46*, 1216; b) M. R. Palacin, *Chem. Soc. Rev.* **2009**, *38*, 2565; c) K. J. Griffith, K. M. Wiaderek, G. Cibir, L. E. Marbella, C. P. Grey, *Nature* **2018**, *559*, 556; d) Y. He, A. Muhetaer, J. Li, F. Wang, C. Liu, Q. Li, D. Xu, *Adv. Energy Mater.* **2017**, *7*, 1700950.
- [7] a) D. Cao, Z. Yao, J. Liu, J. Zhang, C. Li, *Energy Storage Mater.* **2018**, *11*, 152; b) D. Chen, J. H. Wang, T. F. Chou, B. Zhao, M. A. El-Sayed, M. Liu, *J. Am. Chem. Soc.* **2017**, *139*, 7071.
- [8] J. G. Weissman, E. I. Ko, P. Wynblatt, J. M. Howe, *Chem. Mater.* **1989**, *1*, 187.
- [9] V. Augustyn, J. Come, M. A. Lowe, J. W. Kim, P. L. Taberna, S. H. Tolbert, H. D. Abruna, P. Simon, B. Dunn, *Nat. Mater.* **2013**, *12*, 518.
- [10] K. J. Griffith, A. C. Forse, J. M. Griffin, C. P. Grey, *J. Am. Chem. Soc.* **2016**, *138*, 8888.

- [11] A. Le Viet, M. V. Reddy, R. Jose, B. V. R. Chowdari, S. Ramakrishna, *J. Phys. Chem. C* **2010**, *114*, 664.
- [12] a) B. Deng, T. Lei, W. Zhu, L. Xiao, J. Liu, *Adv. Funct. Mater.* **2018**, *28*, 1704330; b) S. Li, C. N. Schmidt, Q. Xu, X. Cao, G. Cao, *ChemNanoMat* **2016**, *2*, 675; c) H. Yang, H. Xu, L. Wang, L. Zhang, Y. Huang, X. Hu, *Chem. - Eur. J.* **2017**, *23*, 4203; d) C. Huang, J. Fu, H. Song, X. Li, X. Peng, B. Gao, X. Zhang, P. K. Chu, *RSC Adv.* **2016**, *6*, 90489; e) H. Li, Y. Zhu, S. Dong, L. Shen, Z. Chen, X. Zhang, G. Yu, *Chem. Mater.* **2016**, *28*, 5753.
- [13] a) E. Lim, C. Jo, M. S. Kim, M.-H. Kim, J. Chun, H. Kim, J. Park, K. C. Roh, K. Kang, S. Yoon, J. Lee, *Adv. Funct. Mater.* **2016**, *26*, 3711; b) L. Yan, G. Chen, S. Sarker, S. Richins, H. Wang, W. Xu, X. Rui, H. Luo, *ACS Appl. Mater. Interfaces* **2016**, *8*, 22213; c) L. Wang, X. Bi, S. Yang, *Adv. Mater.* **2016**, *28*, 7672.
- [14] E. Lim, C. Jo, H. Kim, M.-H. Kim, Y. Mun, J. Chun, Y. Ye, J. Hwang, K.-S. Ha, K. C. Roh, K. Kang, S. Yoon, J. Lee, *ACS Nano* **2015**, *9*, 7497.
- [15] H. Sun, L. Mei, J. Liang, Z. Zhao, C. Lee, H. Fei, M. Ding, J. Lau, M. Li, C. Wang, X. Xu, G. Hao, B. Papandrea, I. Shakir, B. Dunn, Y. Huang, X. Duan, *Science* **2017**, *356*, 599.
- [16] Y. K. Naoaki Kumagai, S. Komaba, N. Koshibab, *J. Electrochem. Soc.* **1999**, *146*, 3203.
- [17] J. Come, V. Augustyn, J. W. Kim, P. Rozier, P. L. Taberna, P. Gogotsi, J. W. Long, B. Dunn, P. Simon, *J. Electrochem. Soc.* **2014**, *161*, A718.
- [18] J. Meng, Z. Liu, C. Niu, L. Xu, X. Wang, Q. Li, X. Wei, W. Yang, L. Huang, L. Mai, *Mater. Horiz.* **2018**, *5*, 78.
- [19] B. D. Yuhua, D. O. Zitoun, P. J. Pauzauskie, R. He, P. Yang, *Angew. Chem.* **2006**, *118*, 434.
- [20] a) C. Chen, Y. Wen, X. Hu, X. Ji, M. Yan, L. Mai, P. Hu, B. Shan, Y. Huang, *Nat. Commun.* **2015**, *6*, 6929; b) J. Meng, C. Niu, L. Xu, J. Li, X. Liu, X. Wang, Y. Wu, X. Xu, W. Chen, Q. Li, Z. Zhu, D. Zhao, L. Mai, *J. Am. Chem. Soc.* **2017**, *139*, 8212.
- [21] M. V. Reddy, R. Jose, A. Le Viet, K. I. Ozoemena, B. V. R. Chowdari, S. Ramakrishna, *Electrochim. Acta* **2014**, *128*, 198.
- [22] a) Y. Zhang, Z.-B. Wang, F.-D. Yu, L.-F. Que, M.-J. Wang, Y.-F. Xia, Y. Xue, J. Wu, *J. Power Sources* **2017**, *358*, 1; b) X. H. Rui, N. Ding, J. Liu, C. Li, C. H. Chen, *Electrochim. Acta* **2010**, *55*, 2384.
- [23] a) H. Liu, F. C. Strobridge, O. J. Borkiewicz, K. M. Wiaderek, K. W. Chapman, P. J. Chupas, C. P. Grey, *Science* **2014**, *344*, 1252817; b) K.-W. Nam, S.-M. Bak, E. Hu, X. Yu, Y. Zhou, X. Wang, L. Wu, Y. Zhu, K.-Y. Chung, X.-Q. Yang, *Adv. Funct. Mater.* **2013**, *23*, 1047; c) C. Niu, X. Liu, J. Meng, L. Xu, M. Yan, X. Wang, G. Zhang, Z. Liu, X. Xu, L. Mai, *Nano Energy* **2016**, *27*, 147.
- [24] a) J. M. Clark, S. Nishimura, A. Yamada, M. S. Islam, *Angew. Chem., Int. Ed.* **2012**, *51*, 13149; b) A. A. Lubimtsev, P. R. C. Kent, B. G. Sumpter, P. Ganesh, *J. Mater. Chem. A* **2013**, *1*, 14951.
- [25] a) D. J. G. Kresse, *Phys. Rev. B* **1999**, *59*, 1758; b) J. F. G. Kresse, *Phys. Rev. B* **1996**, *54*, 11169; c) J. F. G. Kresse, *Comput. Mater. Sci.* **1996**, *6*, 15.
- [26] a) G. A. B. S. L. Dudarev, S. Y. Savrasov, C. J. Humphreys, A. P. Sutton, *Phys. Rev. B* **1998**, *57*, 1505; b) J. P. Perdew, K. Burke, M. Ernzerhof, *Phys. Rev. Lett.* **1996**, *77*, 3865.
- [27] H. J. Monkhorst, J. D. Pack, *Phys. Rev. B* **1976**, *13*, 5188.
- [28] G. Henkelman, B. P. Uberuaga, H. Jónsson, *J. Chem. Phys.* **2000**, *113*, 9901.
- [29] a) D. Su, H. Ahn, G. Wang, *Appl. Phys. Lett.* **2011**, *99*, 141909; b) D. Morgan, A. Van der Ven, G. Ceder, *Electrochem. Solid-State Lett.* **2004**, *7*, 30.
- [30] G. Henkelman, A. Arnaldsson, H. Jónsson, *Comput. Mater. Sci.* **2006**, *36*, 354.